Bulletin of the Seismological Society of America, Vol. 101, No. 2, pp. 742–755, April 2011, doi: 10.1785/0120100090

Ⓔ

An Empirically Calibrated Framework for Including the Effects of Near-Fault Directivity in Probabilistic Seismic Hazard Analysis

by Shrey K. Shahi and Jack W. Baker

Abstract Forward directivity effects are known to cause pulselike ground motions at near-fault sites. We propose a comprehensive framework to incorporate the effects of near-fault pulselike ground motions in probabilistic seismic hazard analysis (PSHA) computations. Also proposed is a new method to classify ground motions as pulselike or non-pulselike by rotating the ground motion and identifying pulses in all orientations. We have used this method to identify 179 recordings in the Next Generation Attenuation (NGA) database (Chiou *et al.*, 2008), where a pulselike ground motion is observed in at least one orientation. Information from these 179 recordings is used to fit several data-constrained models for predicting the probability of a pulselike ground motion occurring at a site, the orientations in which they are expected relative to the strike of the fault, the period of the pulselike feature, and the response spectrum amplification due to the presence of a pulselike feature in the ground motion. An algorithm describing how to use these new models in a modified PSHA computation is provided. The proposed framework is modular, which will allow for modification of one or more models as more knowledge is obtained in the future without changing other models or the overall framework. Finally, the new framework is compared with existing methods to account for similar effects in PSHA computation. Example applications are included to illustrate the use of the proposed framework, and implications for selection of ground motions for analysis of structures at near-fault sites are discussed.

Online Material: Ground-motion recordings identified as pulselike by the pulse classification algorithm.

Introduction

Ground motions with a pulse at the beginning of the velocity time history belong to a special class of ground motion that causes severe damage in structures. This type of ground motion, referred to in this paper as a pulselike ground motion, is typically observed at sites located near the fault and is believed to be caused primarily by forward directivity effects (Somerville *et al.*, 1997; Somerville, 2003, 2005; Spudich and Chiou, 2008). Pulselike ground motions place extreme demands on structures and are known to have caused extensive damage in previous earthquakes (e.g., Bertero *et al.*, 1978; Anderson and Bertero, 1987; Hall *et al.*, 1995; Iwan, 1997; Alavi and Krawinkler, 2001; Menun and Fu, 2002; Makris and Black, 2004; Mavroeidis *et al.*, 2004; Akkar *et al.*, 2005; Luco and Cornell, 2007). Traditional ground-motion models used in probabilistic seismic hazard analysis (PSHA) (e.g., Kramer, 1996; McGuire, 2004) do not account for the effects of pulselike ground motions and may therefore underpredict the seismic hazard at near-fault sites where pulselike ground motions are expected. In order to correctly assess the seismic hazard at near-fault sites, it is important to model the effects of pulselike ground motion and incorporate these effects in hazard calculations. Another near-fault effect called fling step, which causes permanent ground displacement, is mentioned for completeness but is not considered in this paper.

Few attempts have been made in the past to incorporate the effect of near-fault pulses in seismic hazard assessment. These past efforts have tried to model the amplification of response spectra due to pulselike motion either by monotonically increasing or decreasing the spectral ordinates over a range of periods (e.g., Somerville *et al.*, 1997; Abrahamson, 2000) or by amplifying the response spectra in a narrow range of periods close to the period of pulse (T_p) (e.g., Somerville, 2005; Tothong *et al.*, 2007). The former models are sometimes referred to as broadband models, the latter as narrowband models. The framework proposed here extends the approach proposed by Tothong *et al.* (2007) and uses data-constrained models for all calculations rather than the hypothetical models used in some cases in that effort. The proposed framework also allows for computation of PSHA results for arbitrary orientations relative to surrounding faults. The model proposed here can be categorized as a narrowband model, as the spectral acceleration is amplified in a range of periods centered about the period of the pulse, but no assumptions about the level of amplification or the range of periods to be amplified were made beforehand. Instead, the model was calibrated purely empirically. A modified version of the algorithm suggested by Baker (2007) is used here to classify pulselike ground motions. The modified algorithm rotates the ground motion and identifies pulses in all orientations rather than only in the fault-normal direction. This modification allows identification of velocity pulses in arbitrary orientations, which are then used to calibrate the needed predictive models.

The complete framework includes models for predicting the probability of pulse occurrence for a given source-site geometry, the probability of observing a pulse in a particular orientation given a pulse is observed at the site, the distribution of period of the pulse, the amplification of the response spectra due to the presence of the pulse, and the deamplification of response spectra due to absence of pulse in near-fault ground motion. Example calculations are included, which suggest some of the ways in which the framework proposed here can be used.

Identification of Pulselike Ground Motions

In order to complete a probabilistic study of pulselike ground motions, a library of ground motions is needed, with each ground motion classified as pulselike or non-pulselike. Many researchers have developed libraries of pulselike ground motions by classifying ground motions using visual or quantitative techniques (e.g., Mavroeidis and Papageorgiou, 2003; Someville, 2003; Fu and Menun, 2004; Akkar *et al.*, 2005). These documents do not provide non-pulselike ground motions, preventing analysts from determining the likelihood of pulse occurrence.

We preferred the pulse classification algorithm suggested in Baker (2007) because it is a completely quantitative method and allows classification of a large dataset such as the Next Generation Attenuation (NGA) database (Chiou *et al.*, 2008) without human intervention. The Baker (2007) algorithm uses wavelet analysis to extract the pulselike feature from the velocity time history of the fault-normal component of the ground motion. The extracted pulselike feature is then analyzed and is used to classify the ground motion as pulselike or non-pulselike. Although classification of some records into binary criteria of pulselike and non-pulselike is difficult, this algorithm is generally effective at providing defensible classifications. Figure 1 graphically illustrates the algorithm results.

Although velocity pulses caused by directivity effects are expected to be found in the fault-normal component of the ground motion (Somerville *et al.*, 1997), many fault ruptures have irregular geometry, which makes determination of exact fault-normal direction difficult. Pulselike ground motions are also observed in a range of orientations (e.g., Howard *et al.*, 2005). To illustrate, Figure 2 shows the pulse indicator score as computed by the Baker (2007) algorithm at a site in different orientations (pulselike ground motions have high pulse indicator values). The pulse indicator scores in Figure 2 show that pulselike ground motions

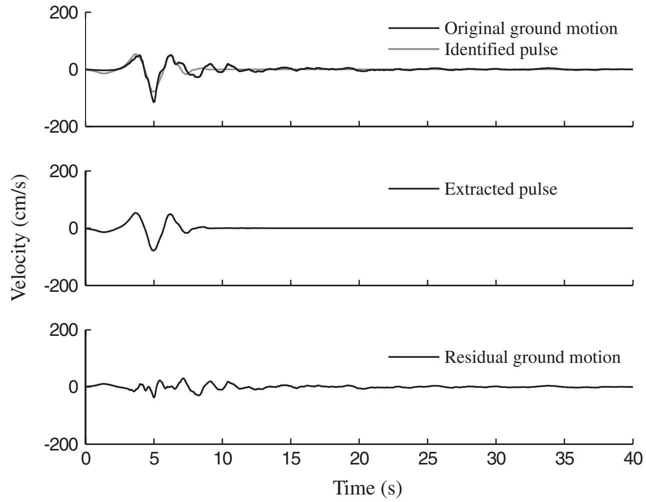

Figure 1. Illustration of the procedure used by the Baker (2007) algorithm to extract the largest pulse from a velocity time history (1979 Imperial Valley, El Centro (EC) Meloland Overpass recording). In this case the pulse is large and the ground motion is classified as pulselike.

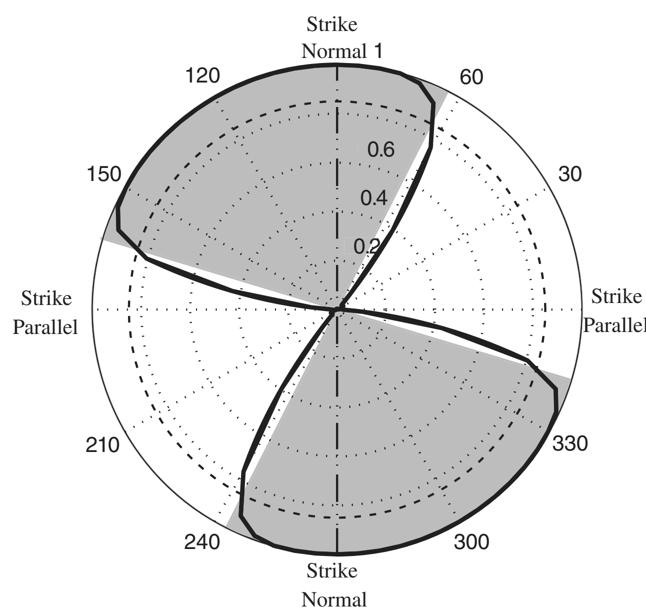

Figure 2. Pulse indicator values as a function of orientation for the 1979 Imperial Valley, EC County Center recording. Shaded areas indicate orientations in which a strong pulse is apparent. For more information on how pulse indicator is calculated, see Baker (2007).

occurred in a range of orientations. The case illustrated in Figure 2 is a simple case where pulses are observed around the strike-normal orientation. More complex cases exist where the strike-normal orientation does not lie in the range of orientation in which pulses were observed but these cases are small in number.

In order to study the orientations in which pulselike ground motions are observed, the ground motions were rotated in all possible orientations, and the ground motion in each orientation was classified as pulselike or non-pulselike. A site was then deemed to have experienced a pulselike ground motion if the ground motion in any orientation at the site was classified as pulselike. This scheme of rotating and classifying ground motions in every orientation led to the identification of 179 recordings in the NGA database that experienced pulselike ground motion. For a list of these 179 recordings, see Ⓔ Table S1 in the electronic supplement to this paper. This classification scheme identifies pulses in the horizontal directions only and may not classify some pulselike ground motions when the pulse lies out of the horizontal plane. The fault-normal orientation may not lie in the horizontal plane for some non-strike-slip faults; thus, the non-strike-slip models developed in this paper should only be used when out of horizontal plane pulses are not important.

The previous study by Baker (2007), which studied only fault-normal ground motions, identified 91 pulselike ground motions from the same database used here. Most of the additional pulselike ground motions identified here were found to have a visual pulselike feature in the strike-normal direction. These were not classified as pulselike in the previous study by Baker (2007) because the pulselike feature in the strike-normal direction narrowly missed the thresholds used for classification. The presence of a visual pulse in the velocity time history of the strike-normal direction of most of the ground motions we classified as pulselike suggests that directivity effects may be the chief cause of the pulselike feature in these ground motions.

Development of Input Models for Modified PSHA

The conventional PSHA equation shown in equation (1)

$$\nu_{S_a}(x) = \sum_{i=1}^{\#\text{faults}} \nu_i \iint P(S_a > x|m, r) \cdot f_i(m, r) \cdot dm \cdot dr, \tag{1}$$

is used to find the annual rate by which S_a (the associated period T is omitted from the notation here for brevity) at the site exceeds a value x (for more details see, e.g., Kramer, 1996; McGuire, 2004). The term $P(S_a > x|m, r)$ provides the probability that S_a at a given period exceeds a value of x given the occurrence of an earthquake of magnitude m at distance r, which can be calculated using any ground-motion model. This probability, when multiplied by $f_i(m, r)$, the probability density of occurrence of such an earthquake (of magnitude m, and distance r) on a particular fault i, and integrated over all possible m and r values, gives the probability of exceedance given an earthquake on a single fault. The total exceedance rate at a site can then be found by multiplying this probability by the rate of occurrence of earthquakes on the fault, ν_i, and summing over each fault the vicinity of the site. Note that the probability $P(S_a > x|m, r)$ is obtained using a ground-motion model that is in general also a function of parameters such as rupture mechanism, site conditions, and parameters other than magnitude and distance, but those parameters are omitted from the notation here for brevity.

The effects of pulselike ground motion can be included in hazard analysis by using a modified ground-motion model that accounts for the amplification effect of directivity pulses on S_a values. Because directivity effects depend mainly on source-site geometry (Somerville *et al.*, 1997), the ground-motion model accounting for pulses needs to be a function of source-site geometry along with magnitude and distance. So a modified ground-motion model that accounts for pulselike ground motions can be used to calculate the probability of exceedance, $P^*(S_a > x|m, r, z)$, where z represents the source-to-site geometry information. This new probability of exceedance, $P^*(S_a > x|m, r, z)$, when used in the PSHA equation, can give the rate of exceedance of S_a at the site after accounting for effects of pulselike ground motions.

Equation (2) shows how directivity effects can be accounted for in a PSHA calculation:

$$\nu_{S_a}(x) = \sum_{i=1}^{\#\text{faults}} \nu_i \iiint P^*(S_a > x|m, r, z) \cdot f_i(m, r, z) \cdot dm \cdot dr \cdot dz. \tag{2}$$

Note that this equation follows the proposal of Tothong *et al.* (2007); additional details can be found there.

The presence of a pulselike feature in the ground motion amplifies the response spectrum for a range of periods, as can be seen in Figure 3. This amplification of response significantly raises the probability of exceeding a particular S_a level when pulselike ground motion occurs at a site. Therefore, the PSHA equation proposed here (equation 2) can be practically evaluated by splitting $P^*(S_a > x|m, r, z)$ into two cases, depending on whether or not pulselike ground motion is observed. These two cases can then be combined to calculate the overall exceedance rate, as explained in the following paragraphs.

The current ground-motion models are fitted empirically using both pulselike and non-pulselike ground motions from a ground motion database. In the near-fault region, where pulses are mostly observed, the ground-motion models may underpredict the pulselike ground motion and overpredict the non-pulselike ground motion. When a pulse is observed, a prediction of S_a exceedance can be obtained from

$$P(S_a > x|m, r, z, \text{pulse}) = 1 - \Phi\left(\frac{\ln(x) - \mu_{\ln S_{a,\text{pulse}}}}{\sigma_{\ln S_{a,\text{pulse}}}}\right), \tag{3}$$

where the pulselike ground motions have mean $\mu_{\ln S_{a,\text{pulse}}}$ and standard deviation $\sigma_{\ln S_{a,\text{pulse}}}$. Note that $\mu_{\ln S_{a,\text{pulse}}}$ and

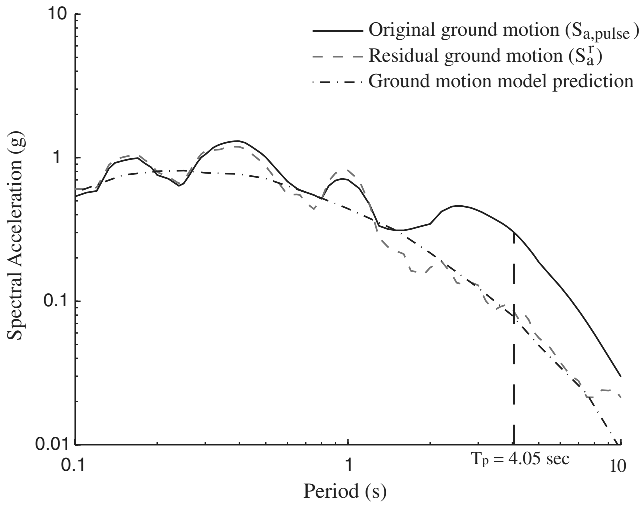

Figure 3. Response spectra of the 1979 Imperial Valley, El Centro Array # 5 ground motion in fault-normal orientation. The Boore and Atkinson (2007) median prediction and the response spectra from residual ground motion are also shown.

$\sigma_{\ln S_{a,\text{pulse}}}$ are functions of m, r, T_p, and other factors, but that dependence has again been omitted for brevity in order to highlight the aspects of the calculation that are new in this paper.

In the second case, when no pulse is observed, a modified ground-motion model after correcting for the overprediction can be used to compute the probability of S_a exceeding x

$$P(S_a > x|m, r, \text{no pulse}) = 1 - \Phi\left(\frac{\ln(x) - \mu_{\ln S_{a,\text{no pulse}}}}{\sigma_{\ln S_{a,\text{no pulse}}}}\right), \tag{4}$$

where the mean value $\mu_{\ln S_{a,\text{no pulse}}}$ and standard deviation $\sigma_{\ln S_{a,\text{no pulse}}}$ can be estimated using a modified ground-motion model for non-pulselike ground motions. In both equations (3) and (4) $\Phi()$ represents the standard normal cumulative distribution function. A normal distribution of residuals was assumed, and histograms of the residuals from the model presented in this paper are consistent with that assumption.

These two cases can be combined using the total probability theorem (e.g., Benjamin and Cornell, 1970) to get the overall probability of S_a exceeding x at a site

$$\begin{aligned} &P^*(S_a > x|m, r, z) \\ &\quad = P(\text{pulse}|m, r, z) \cdot P(S_a > x|m, r, z, \text{pulse}) \\ &\qquad + (1 - P(\text{pulse}|m, r, z)) \cdot P(S_a > x|m, r, \text{no pulse}). \end{aligned} \tag{5}$$

The following sections will present empirically calibrated models for the terms required in equations (2) to (5).

Probability of Observing a Pulse

As seen in equation (5), the probability of observing a pulselike ground motion at a site is needed for the proposed PSHA calculation. We used a logistic regression model for predicting the probability of pulse occurrence given the source-site geometry. Logistic regression is a generalized linear model used for fitting binomial data (e.g., Kutner *et al.*, 2004).

It has been well established that the forward directivity effect, which is believed to be a cause of pulselike ground motions, depends on the source-to-site geometry (Somerville *et al.*, 1997). Iervolino and Cornell (2008) showed that the parameters r, s, and θ for strike-slip faults, and r, d, and ϕ for non-strike-slip faults have better predictive power than other parameters when used in logistic regression to compute the probability of pulse occurrence. Figure 4 graphically explains these parameters. We used the same parameters selected by Iervolino and Cornell (2008) to fit the logistic regression using information from all the sites in the NGA database. Refitting of the model was required because the Iervolino and Cornell (2008) model only predicts the probability of observing pulses in the fault-normal direction while we need a model to predict pulses in any orientation. We found that only r and s were statistically significant predictors in the case of strike-slip earthquakes, whereas r, d, and ϕ were statistically significant in the non-strike-slip case. The result of the logistic regression is summarized by equations (6) and (7):

$$P(\text{pulse}|r, s) = \frac{1}{1 + e^{(0.642+0.167\cdot r-0.075\cdot s)}} \quad \text{for strike-slip} \tag{6}$$

and

$$P(\text{pulse}|r, d, \phi) = \frac{1}{1 + e^{(0.128+0.055\cdot r-0.061\cdot d+0.036\cdot\phi)}} \quad \text{for non-strike-slip.} \tag{7}$$

Here the units of r, d, and s are kilometers and ϕ is degrees. The dataset used for fitting contained r ranges from 0.3 km to

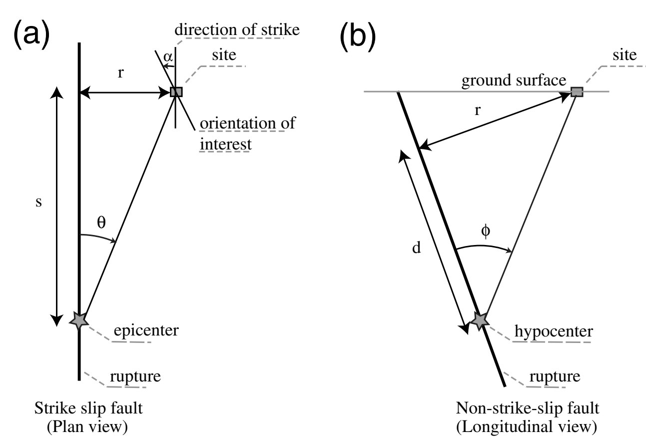

Figure 4. Plot explaining the parameters needed to fit the logistic regression for (a) strike-slip and (b) non-strike-slip faults. The parameter α, the angle between orientation of interest and the strike of the fault, is also shown.

255 km in the case of non-strike-slip ruptures and 0.07 km to 472 km in the case of strike-slip ruptures, d ranges from 0 km to 70 km, ϕ ranges from 0 to 90 degrees, and s ranges from 0.3 km to 143 km.

A contour map of these predicted probabilities for a strike-slip fault is shown in Figure 5a and for a non-strike-slip fault in Figure 6a. Contours in the maps show the probability of pulse occurrence as predicted around the rupture geometries associated with the Imperial Valley earthquake and the Northridge earthquake. These maps can be compared with the actual maps of sites where pulselike ground motions were observed during the Imperial Valley earthquake, shown in Figure 5b and the Northridge earthquake, shown in Figure 6b. The model predicts high probability of pulses in regions where directivity effects were observed, and the shape of the contours also appears to be consistent with actual observations.

Pulse Orientation

Rotating and classifying ground motions led to identification of pulselike ground motions in a range of orientations. To calculate hazard for a site with nearby faults at multiple orientations, one must know the probability of observing a pulselike ground motion in an arbitrary direction. The data from rotated pulse classifications was used to determine the probability of finding a pulse in a direction (α) given that a pulse is observed at the site, that is, $P(\text{pulse at } \alpha|\text{pulse})$. The angle α represents the smallest angle measured with respect to strike of the fault (strike values were taken from the NGA database). Figure 4a shows a schematic diagram illustrating α. We found that $P(\text{pulse at } \alpha|\text{pulse})$ was different for strike-slip and non-strike-slip faults.

Figure 7 shows the fraction of pulselike motions containing a pulse in orientation α for strike-slip and non-strike-slip faults. The figure also shows the model that was fitted by minimizing squared errors between observation and prediction. The model is given in equations (8) and (9) for strike-slip and non-strike-slip faults, respectively:

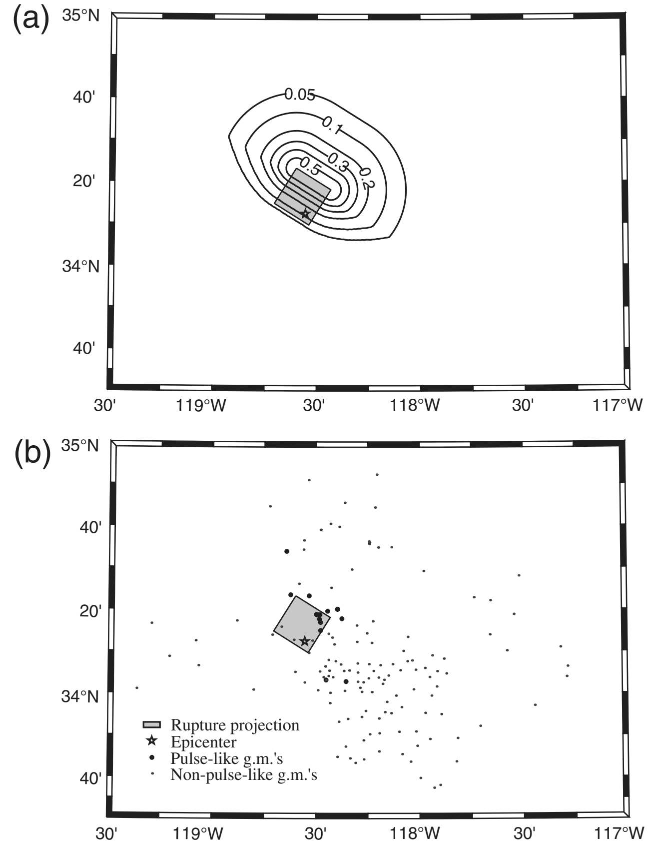

Figure 6. Map of the Northridge earthquake showing (a) contours of probability of pulse occurrence for the given rupture, and (b) sites where pulselike ground motion was observed.

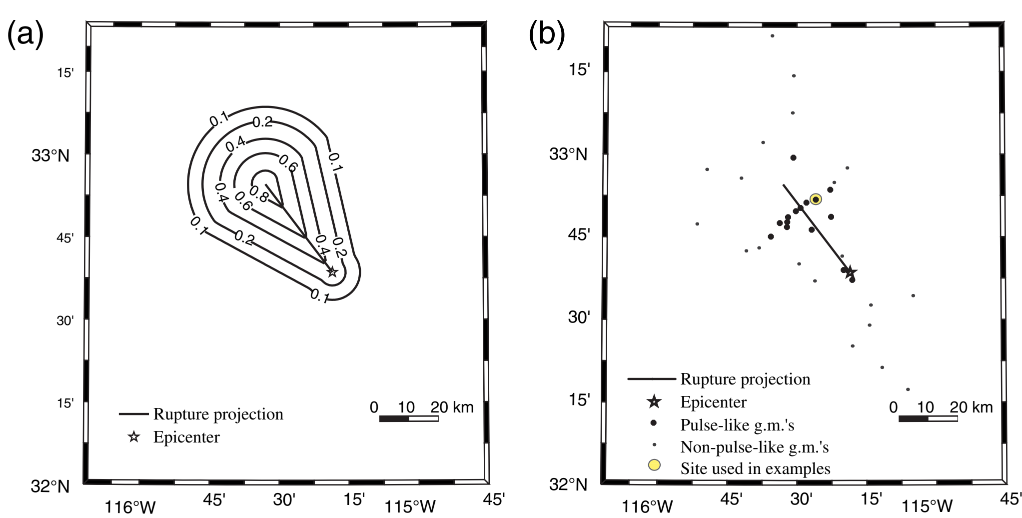

Figure 5. Map of the Imperial Valley earthquake showing (a) contours of probability of pulse occurrence for the given rupture, and (b) sites where pulselike ground motion was observed. The site within the shaded circle is the one for which example hazard analysis is done. The color version of this figure is available only in the electronic edition.

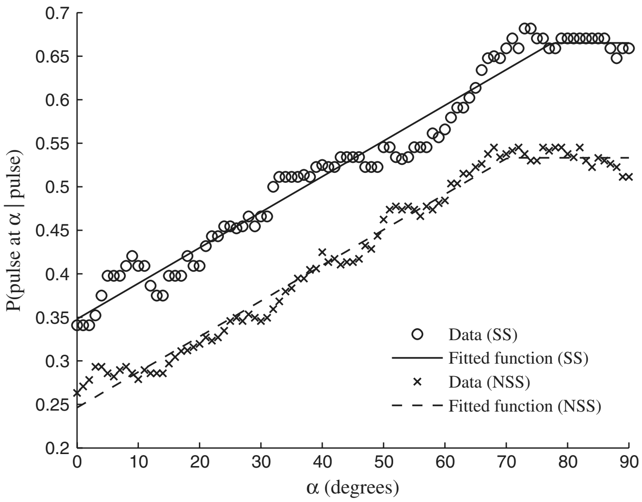

Figure 7. Plot of probability of pulse at α given pulse at site for both strike-slip (SS) and non-strike-slip (NSS) faults.

$$P(\text{pulse at }\alpha|\text{pulse}) = \min[0.67, 0.67 - 0.0041 \cdot (77.5 - \alpha)] \quad \text{for strike-slip} \tag{8}$$

and

$$P(\text{pulse at }\alpha|\text{pulse}) = \min[0.53, 0.53 - 0.0041 \cdot (70.2 - \alpha)] \quad \text{for non-strike-slip.} \tag{9}$$

Because the directivity effect is strongest in the fault-normal orientation, and the strike-normal orientation is generally close to projection of fault-normal orientation in horizontal plane, it is expected to have higher probability of observing a pulse compared to other orientations. As expected, these results show that the most likely orientation to find a pulselike ground motion is normal to the strike ($\alpha = 90$), while the least likely orientation is parallel to the strike ($\alpha = 0$) for both strike-slip and non-strike-slip faults.

The probability of observing a pulselike ground motion at a site in a direction α degrees from the strike of the fault segment can be expressed by

$$P(\text{pulse at }\alpha) = P(\text{pulse at }\alpha|\text{pulse}) \cdot P(\text{pulse}), \tag{10}$$

where terms on the right side of the equation are defined by equations (6) through (9).

Period of the Pulse

The amplification of spectral acceleration (S_a) due to the presence of a pulselike feature in a ground motion depends on the period of the pulse. Many researchers have found in the past that the pulse period depends on the magnitude of the earthquake and have modeled this relationship (Mavroeidis and Papageorgiou, 2003; Somerville, 2003; Bray and Rodriguez-Marek, 2004; Baker, 2007). Because by using the modified classification algorithm we identified many ground motions with pulses that had not been used in previous studies, we modeled the relationship between pulse period and magnitude using all the pulses classified in this study.

In order to determine the relationship between pulse period and magnitude of the earthquake, the periods of all of the identified pulses were computed. The period associated with the maximum Fourier amplitude of the extracted pulse was used as a measure of the period of the pulse for this study, following Baker (2007). Linear regression between $\ln T_p$ and magnitude gave the relationship shown in equations (11) and (12)

$$\mu_{\ln T_p} = -5.73 + 0.99M \tag{11}$$

and

$$\sigma_{\ln T_p} = 0.56. \tag{12}$$

Figure 8 shows the observed T_p and M values along with the relationship given in equation (11). The residuals from this model fit a normal distribution well, so $\ln T_p$ can be assumed to be normally distributed (or T_p log-normally distributed), with mean ($\mu_{\ln T_p}$) given by the prediction from equation (11), and standard deviation ($\sigma_{\ln T_p}$) given by equation (12).

Figure 8 shows that the number of pulselike ground motions with low T_p are small. Values of $T_p < 0.6$ s are rare and directivity pulses with these low periods are not expected to contribute significantly to seismic hazard. Thus, $T_p < 0.6$ s observations are ignored in these models and later calculations.

Amplification of Spectral Acceleration due to Presence of Pulse

The proposed framework requires a ground-motion model that accounts for pulselike features. The ground-motion model for the case when pulse is observed needs to predict mean and standard deviation of $\ln S_{a,\text{pulse}}$ at the site. In order

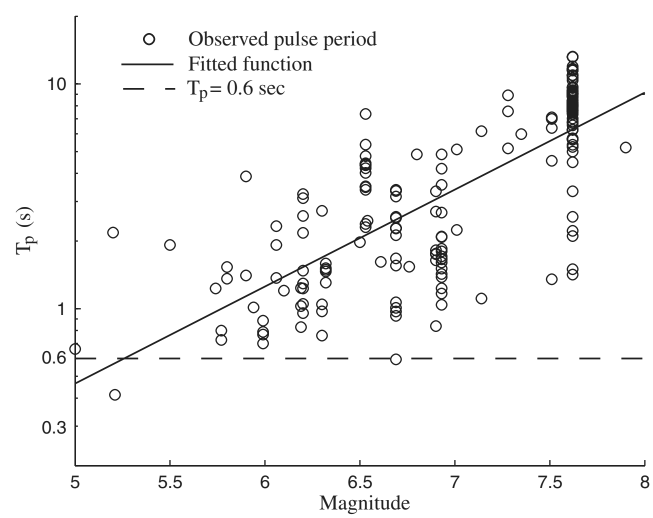

Figure 8. Pulse period versus earthquake magnitude for observed pulselike ground motions.

to simplify the model, $\ln S_{a,\text{pulse}}$ can be broken down into two parts

$$\ln S_{a,\text{pulse}} = \ln\left(\frac{S_{a,\text{pulse}}}{S_a^r} \cdot S_a^r\right), \tag{13}$$

$$= \ln(Af \cdot S_a^r), \tag{14}$$

$$= \ln Af + \ln S_a^r. \tag{15}$$

The S_a^r term in equation (15) is the spectral acceleration of the residual ground-motion (i.e., the ground-motion after the observed pulse is removed, discussed previously), and Af is the amplification factor due to the presence of a pulse (i.e., $Af = S_{a,\text{pulse}}/S_a^r$). This representation of the ground-motion model allows us to model the amplification due to the pulselike feature and the residual ground motion at a site separately. Figure 3 shows $S_{a,\text{pulse}}$ and S_a^r for a pulselike ground motion.

Figure 9 shows the epsilons (ϵ) of the residual ground motion with respect to the Boore and Atkinson (2008) model (referred to as BA2008 hereafter). The ϵ is the standardized residual of the BA2008 model prediction and will be discussed in more detail later. The figure shows that the mean ϵ is close to zero, suggesting that the ground-motion model is good at predicting S_a^r on average, and thus may be used to model the residual ground motions. Chioccarelli and Iervolino (2010) found that the fault-normal component is sometimes stronger than the fault parallel one even after removal of the pulse; the result shown in Figure 9 is consistent with this finding as the ϵ from residual ground motion are positive (i.e., the residual ground motion is stronger than the prediction on average), but the ϵ are close enough to zero that we can assume that traditional ground-motion models can be used to predict the residual ground motion. So equation (15) can be rewritten, replacing the $\ln S_a^r$ by prediction from traditional ground-motion models ($\ln S_{a,\text{gmm}}$):

$$\ln S_{a,\text{pulse}} = \ln Af + \ln S_{a,\text{gmm}}. \tag{16}$$

We computed amplification factors as the ratio of the S_a from original ground motion to the S_a from residual ground motions. Figure 10a shows the amplification factors plotted against the ratio of the period of interest (T) and period of pulse (T_p). The average amplification forms a bell-shaped pattern centered near to $T/T_p = 1$.

We tested several functional forms and fitted the best among them to data using minimization of the squared errors to obtain the following mean amplification function:

$$\mu_{\ln Af} = \begin{cases} 1.131 \cdot \exp(-3.11 \cdot (\ln(T/T_p) + 0.127)^2) + 0.058 & \text{if } T \leq 0.88 \cdot T_p \\ 0.896 \cdot \exp(-2.11 \cdot (\ln(T/T_p) + 0.127)^2) + 0.255 & \text{if } T > 0.88 \cdot T_p. \end{cases} \tag{17}$$

Figure 10a also shows this fitted model along with the observed amplifications. Amplifications for pulses found in different orientations are plotted in Figure 10b, which shows that the model is stable with respect to change in orientation. Similar tests showed that the amplification due to the presence of a pulse is stable with respect to change in earthquake magnitudes and type of faulting as well. We can take expectations of equation (16) to get

$$\mu_{\ln S_{a,\text{pulse}}} = \mu_{\ln Af} + \mu_{\ln S_{a,\text{gmm}}}. \tag{18}$$

Because the modified ground-motion model presented here is only for pulselike ground motions, we expected the standard deviation within this subset to be lower than the standard deviation of the entire ground-motion library (which contains both pulselike and non-pulselike ground motions). Also, because the modified ground-motion model presented here accounts for the amplification by directivity pulses, this refinement leads to a reduction in standard deviation of the residuals. The observed reduction in standard deviation depends on T/T_p, and is modeled by equation (19):

$$\sigma_{\ln S_{a,\text{pulse}}} = Rf \cdot \sigma_{\ln S_{a,\text{gmm}}}, \tag{19}$$

where Rf, the reduction factor, is modeled as

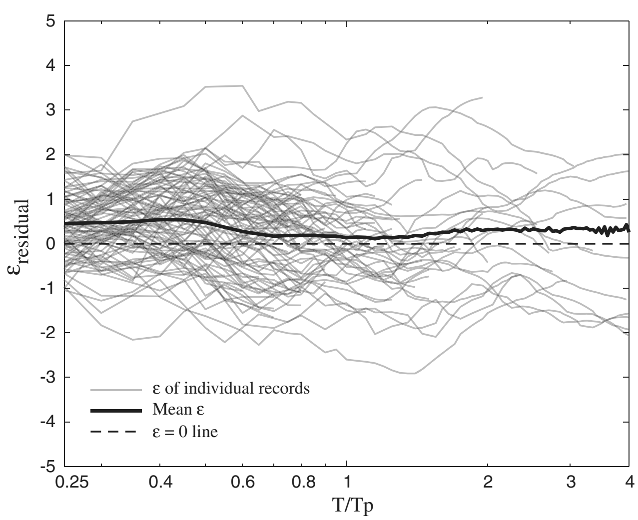

Figure 9. Observed ϵ values of residual ground motions.

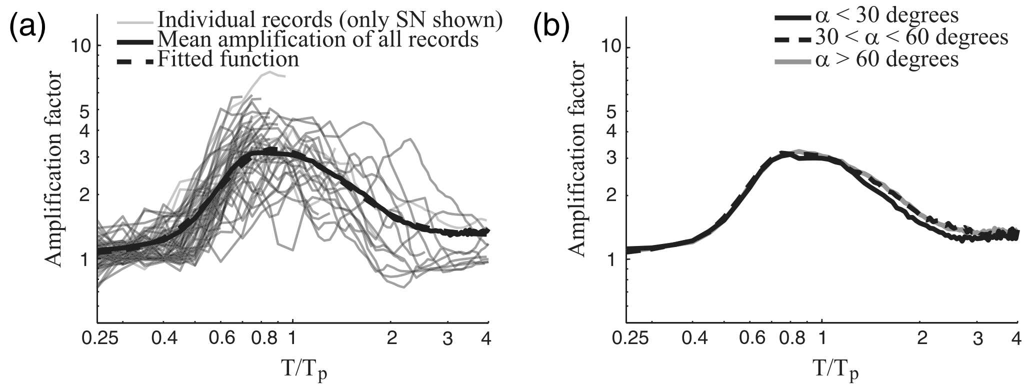

Figure 10. Amplification factor for S_a due to the presence of pulselike features in ground motions. (a) Plot of predictive equation along with the observed data. (b) Mean amplification due to pulses oriented in different directions.

$$Rf = \begin{cases} 1 - 0.2 \cdot \exp(-0.96 \cdot (\ln(T/T_p) + 1.56)^2) & \text{if } T \leq 0.21 \cdot T_p \\ 1 - 0.21 \cdot \exp(-0.24 \cdot (\ln(T/T_p) + 1.56)^2) & \text{if } T > 0.21 \cdot T_p. \end{cases} \tag{20}$$

Figure 11 shows the ratio of standard deviation of residuals from the modified model to that from the BA2008 model.

Note that equations (17) and (20) are strictly empirical fits to observed data. While these equations effectively reproduce the data, physical explanations for these functional forms are not yet available. The results from equations (18) to (20) can be used to evaluate equation (3).

All the results presented in this section are statistically fitted to data and depend on the period of the pulse (T_p). As discussed earlier, observation of $T_p < 0.6$ s is rare and extrapolating the model for cases when $T_p < 0.6$ s will result in amplification at low periods, so we recommend using these results to modify the conventional ground-motion models only for cases when $T_p > 0.6$ s. Note that this limit restricts amplification of S_a at small periods, which is consistent with limits used in some other models (e.g., Somerville *et al.*, 1997; Abrahamson, 2000).

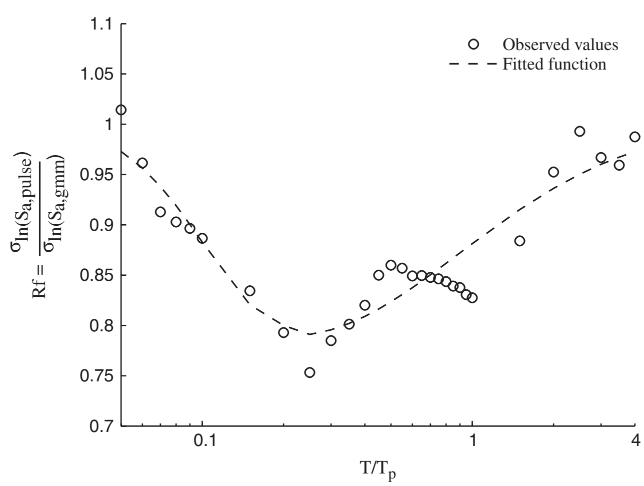

Figure 11. Ratio of standard deviation of residuals from predictions of pulselike spectra ($\sigma_{\ln S_{a,\text{pulse}}}$) to the BA2008 ground-motion model standard deviation ($\sigma_{\ln S_{a,\text{gmm}}}$).

Modification of Ground-Motion Model to Predict Non-Pulselike Ground Motion

The proposed framework requires a ground-motion model to predict the probability of $S_a > x$ given that no pulse is observed at the site. Because the traditional ground-motion models are fitted to both pulselike and non-pulselike ground motions, they are expected to underpredict the spectral accelerations of pulselike ground motions and overpredict the spectral acceleration of non-pulselike ground motions. This underprediction of pulselike ground motions and overprediction of non-pulselike ground motions can be seen in Figure 12, which shows the median prediction (adjusted for the interevent residual) of $S_a(2\text{ s})$ along with observations from the Northridge earthquake. Figure 12 shows that pulselike ground motions generally lie above the median prediction and thus have positive ϵ (i.e., underprediction). Conversely, the non-pulselike ground motions tend to have negative ϵ values (i.e., overprediction). This results in model predictions with ϵ close to zero on average (i.e., unbiased prediction), but here we explicitly correct the under- and overprediction when the pulselike motions are classified.

The overprediction of non-pulselike motion by the ground-motion model is corrected by the same scheme used to correct the ground-motion models for pulselike ground motions. The following equation shows the model used to correct the ground-motion models for the non-pulselike case:

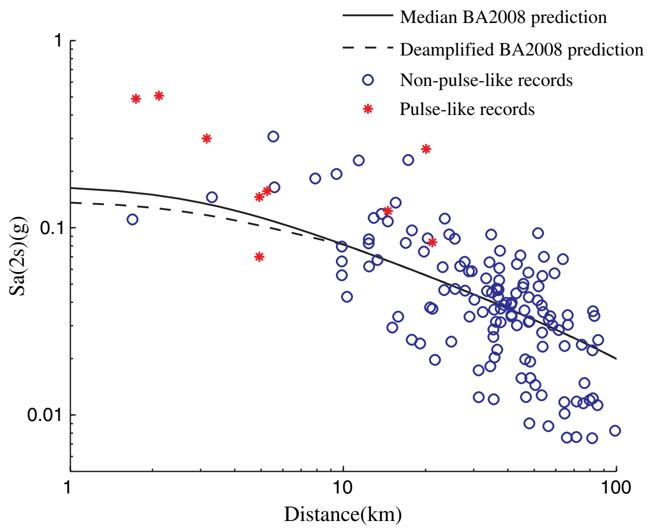

Figure 12. Median $S_a(2\ \mathrm{s})$ prediction from the Boore–Atkinson 2008 model with and without the deamplification along with the actual observations from the Northridge earthquake. The Boore–Atkinson model prediction includes the interevent residual of the Northridge earthquake. The color version of this figure is available only in the electronic edition.

$$\begin{aligned}\ln S_{a,\text{no pulse}} &= \ln\left(\frac{S_{a,\text{no pulse}}}{S_{a,\text{gmm}}} \cdot S_{a,\text{gmm}}\right) \\ &= \ln(Df \cdot S_{a,\text{gmm}}) \\ &= \ln Df + \ln S_{a,\text{gmm}}. \end{aligned} \tag{21}$$

The Df term in equation (21) is the deamplification factor that corrects for the overprediction by the ground-motion models. Df was found to depend on earthquake magnitude and distance from fault. We modeled Df by fitting simple functional forms to observed ϵ values. The deamplification of mean S_a for cases with $T > 1$ s is given by

$$\mu_{\ln Df} = \begin{cases} \max[-0.0905 \cdot \ln T \cdot g_M \cdot g_R, -0.0905 \cdot \ln 2 \cdot g_M \cdot g_R] & \text{for strike-slip} \\ -0.029 \cdot \ln T \cdot g_M \cdot g_R, & \text{for non-strike-slip} \end{cases}, \tag{22}$$

where

$$g_M = \begin{cases} 0 & \text{if } M < 6 \\ (M-6)/0.5 & \text{if } 6 \le M \le 6.5 \\ 1 & \text{if } M \ge 6.5 \end{cases} \tag{23}$$

and

$$g_R = \begin{cases} 10 - r_{\text{jb}} & \text{if } r_{\text{jb}} \le 10\ \text{km} \\ 0 & \text{if } r_{\text{jb}} > 10\ \text{km} \end{cases}, \tag{24}$$

where r_{jb} is the Joyner–Boore distance (closest distance to the surface projection of the fault). When $T \le 1$ s, S_a is not deamplified.

There was little difference between the standard deviation of the residuals computed from the data and those reported in the BA2008 model, so we use the standard deviation from the conventional ground-motion model as the standard deviation for this non-pulselike ground-motion model.

These models can be used along with a conventional ground-motion model to compute $\mu_{\ln S_{a,\text{no pulse}}}$ and $\sigma_{\ln S_{a,\text{no pulse}}}$, as shown in equations (25) and (26):

$$\mu_{\ln S_{a,\text{no pulse}}} = \mu_{\ln Df} + \mu_{\ln S_{a,\text{gmm}}} \tag{25}$$

and

$$\sigma_{\ln S_{a,\text{no pulse}}} = \sigma_{\ln S_{a,\text{gmm}}}. \tag{26}$$

These can then be used to calculate probability of exceedance given that no pulse is observed at the site $[P(Sa > x|m, r, \text{no pulse})]$ by using equation (4). Though this model has been calibrated using the residuals from the BA2008 model, it should be applicable to other ground-motion models, too.

Algorithm to Include the Effects of Pulselike Ground Motion in PSHA

The use of models presented in the Development of Input Models for Modified PSHA section to account for the effect of pulselike ground motions in PSHA is described step-by-step in Table 1. Note that this algorithm for PSHA is a concise version focusing primarily on the modifications to traditional PSHA.

A new variable, z, representing source-to-site geometry, is introduced into the PSHA framework equation given by equation (2). We define the source-to-site geometry using the parameters α, r, and s for strike-slip faults, and α, r, d, and ϕ for non-strike-slip faults, as defined earlier. In order to do a PSHA computation, one needs to sum the hazard over all possible values of z, by iterating over all possible epicenter locations and computing all z parameters for each epicenter location. This is identical to the procedure used by Abrahamson (2000). A uniform distribution of epicenters over rupture length can be used if no other model is preferred, as suggested by Abrahamson (2000).

The amplification in S_a values depends on the period of the pulse, which makes T_p an important variable for hazard computation. T_p should be used as a random variable as explained in the Period of the Pulse section.

The proposed framework allows deaggregation of hazard, to compute the likelihood that an event could have produced the exceedance of a particular threshold S_a value.

Table 1
PSHA Algorithm to Account for Pulselike Ground Motions

T = period of interest
$\nu_{\text{total}} = 0$
$\nu_{\text{pulse}} = 0$
for all faults (fault$_i$) **do**
  α = azimuth of direction of interest − strike direction
  $P = 0$
  $P_{\text{pulse}} = 0$
  for all magnitude (m_j) and distance (r_k) **do**
    compute $P(S_a > x|m_j, r_k, \text{no pulse})$ from equations (4), (25), and (26).
    compute $P(\text{magnitude} = m_j)$ and $P(\text{distance} = r_k)$
    for all positions of epicenter z_l **do**
      compute $P(z = z_l)$
      compute $P(\text{pulse}|m_j, r_k, z_l)$ from equation (6) or (7)
      compute $P(\text{pulse at}\,\alpha|\text{pulse})$ from equation (8) or (9).
      $P(\text{pulse at}\,\alpha) = P(\text{pulse}|m_j, r_k, z_l) * P(\text{pulse at}\,\alpha|\text{pulse})$
      compute $\mu_{\ln T_p}$ and $\sigma_{\ln T_p}$ from equations (11) and (12)
      for all T_p values (t_{pn}) **do**
        compute $P(S_a > x|m_j, r_k, z_l, \text{pulse})$ from equations (3), (18), and (19) for $T_p = t_{pn}$. If $t_{pn} < 0.6$ s, use the unmodified $\mu_{\ln S_{a,\text{gmm}}}$ and $\sigma_{\ln S_{a,\text{gmm}}}$ in place of $\mu_{\ln S_{a,\text{pulse}}}$ and $\sigma_{\ln S_{a,\text{pulse}}}$.
        compute $P^*(S_a > x|m_j, r_k, z_l) = P(\text{pulse at}\,\alpha) * P(S_a > x|m_j, r_k, z_l, \text{pulse}) + (1 - P(\text{pulse at}\,\alpha)) * P(S_a > x|m_j, r_k, \text{no pulse})$
        compute $P(T_p = t_{pn})$ by assuming T_p is log-normally distributed with $\mu_{\ln T_p}$ and $\sigma_{\ln T_p}$
        $P = P + P(\text{magnitude} = m_j) * P(\text{distance} = r_k) * P(z = z_l) * P(T_p = t_{pn}) * P^*(S_a > x|m_j, r_k, z_l)$
        $P_{\text{pulse}} = P_{\text{pulse}} + P(\text{magnitude} = m_j) * P(\text{distance} = r_k) * P(z = z_l) * P(T_p = t_{pn}) * P(S_a > x|m_j, r_k, z_l, \text{pulse}) * P(\text{pulse at}\,\alpha)$
      end for
    end for
  end for
  $\nu_{\text{total}} = \nu_{\text{total}} + \nu_{\text{fault}_i} * P$
  $\nu_{\text{pulse}} = \nu_{\text{pulse}} + \nu_{\text{fault}_i} * P_{\text{pulse}}$
end for

Conventional PSHA allows magnitude, distance, and epsilon (ϵ) deaggregation. The framework proposed here can also be used to perform T_p deaggregation and compute the likelihood that a pulselike ground motion caused the exceedance of a particular S_a value [i.e., $P(\text{pulse}|S_a > x)$].

The $P(\text{pulse}|S_a > x)$ can be calculated by deaggregation of hazard using ν_{pulse} and ν_{total} as shown by

$$P(\text{pulse}|S_a > x) = \frac{P(S_a > x|\text{pulse}) \cdot P(\text{pulse})}{P(S_a > x)} = \frac{\nu_{\text{pulse}}(x)}{\nu_{\text{total}}(x)}, \quad (27)$$

where ν_{pulse} represents the rate of exceedance of S_a by pulselike ground motions only and ν_{total} represents the overall rate of exceedance.

Example Calculations

Several models have been proposed in this paper for different aspects of near-fault pulselike ground motions. In the following paragraphs we present some example calculations using these models.

PSHA for a Single Site

Full probabilistic seismic hazard analysis was done for the site shown on the map in Figure 5. The site and fault parameters were chosen to mimic the conditions at a site that experienced pulselike ground motion during the 1979 Imperial Valley earthquake. Earthquakes of magnitude 5 to 7 were considered, and the characteristic magnitude-recurrence relationship of Youngs and Coppersmith (1985) was used to model the probability distribution of magnitudes. The site is located at a distance 6.7 km from the fault, and the fault is assumed to have a recurrence rate of 0.09 earthquakes per year. Rupture lengths of earthquakes were a function of magnitude, as determined using Wells and Coppersmith (1994). Uniformly distributed hypocenters along the rupture were assumed for PSHA computations. Hazard analysis is performed for the strike-normal orientation ($\alpha = 90$) at the site.

Probabilistic seismic hazard analysis was performed for a range of periods, and both with and without consideration

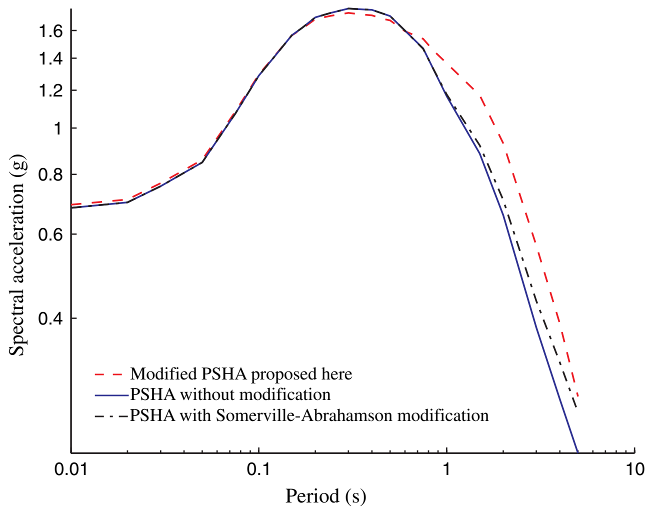

Figure 13. Two percent in 50-year uniform hazard spectra from ordinary PSHA, PSHA with pulse modification suggested in this paper, and PSHA with modification suggested by the Somerville–Abrahamson model for comparison. The color version of this figure is available only in the electronic edition.

around a given pulse period. Figure 13 shows that the model proposed here predicts a bumplike amplification in the uniform hazard spectrum that is broader than the original narrowband amplification (a direct result of considering T_p as a random variable). Note that the range of periods being amplified will be a function of surrounding seismic sources, as predicted pulse periods vary as a function of the earthquake magnitude causing the ground motion. Probabilistic seismic hazard analysis results from a narrowband model such as that proposed here are believed to superior to those from a broadband model (Somerville, 2005). Note that the uniform hazard spectrum is used here simply to provide a concise graphical illustration of how ground motions are amplified with varying period. This figure is not meant to imply that any single ground motion will have such a spectrum, because the uniform hazard spectrum by definition envelopes spectral values from many ground motions having varying magnitudes, distances, and pulse periods, which spreads the amplification due to pulses over a large range of periods. The spectra from a single ground motion will experience amplification in a narrower band of periods.

of the modifications proposed here. To summarize these results graphically, the 2% in the 50-year uniform hazard spectrum from PSHA analysis is shown in Figure 13, along with the uniform hazard spectrum from ordinary PSHA. A third spectrum is shown based on calculations from the Somerville *et al.* (1997) model, later modified by Abrahamson (2000) (this approach will be referred to as the Somerville–Abrahamson model hereafter). The Somerville–Abrahamson model is currently the most widely used method to incorporate the effects of directivity pulses in hazard analysis. It is a broadband model that decreases or increases the spectra monotonically with increasing period, in contrast to the model proposed here that predicts a narrowband amplification

Spatial Pattern of PSHA Amplification due to Pulselike Ground Motion

Probabilistic seismic hazard analysis computations were done for a grid of sites around the same fault used in previous example. At each site, amplification due to pulselike ground motions was computed by taking the ratio between S_a value calculated using the proposed PSHA algorithm and the conventional PSHA calculation. The map in Figure 14a shows the contours of the amplification of the S_a(5 s), exceeded with 2% probability in 50 years. The period of 5 s was chosen for analysis as the models compared in this section had a large difference at this period that made the 5 s period an interesting point of comparison.

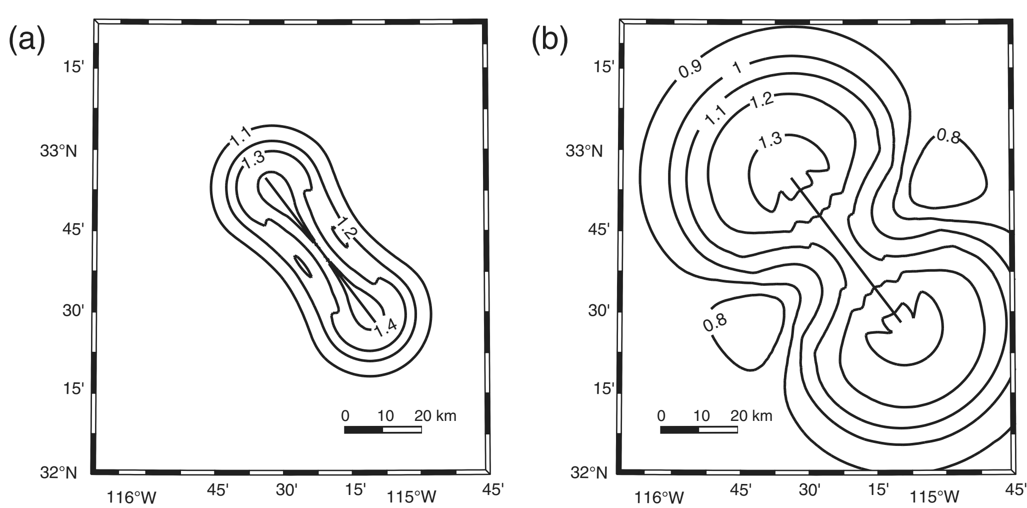

Figure 14. Map showing contours of amplification in 2% in 50-year S_a(5 s) by using (a) modified PSHA described in this paper, and (b) the Somerville–Abrahamson model.

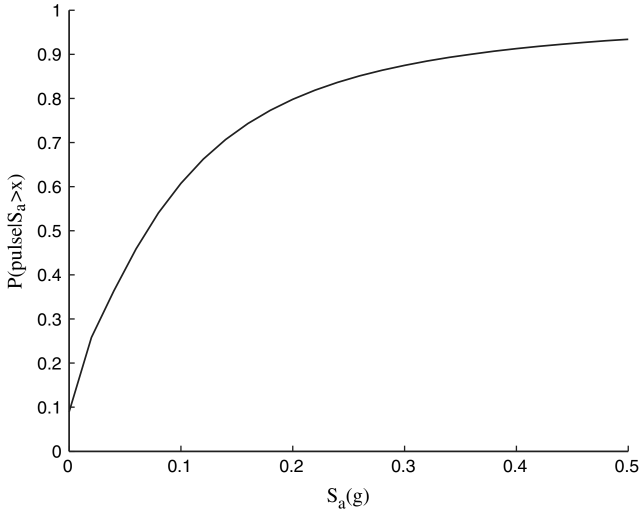

Figure 15. Deaggregation result showing $P(\text{pulse}|S_a \times (5\text{ s}) > x)$.

The contours shown in Figure 14 show high levels of amplification in S_a for sites located near to the fault. This shows that conventional PSHA underpredicts the hazard for near-fault sites, and modification in PSHA to account for effects of near-fault pulse is necessary to correctly assess the hazard at such sites. Similar analysis was done for the Somerville–Abrahamson model to account for directivity. Figure 14b shows the contours of the amplification for 2% in 50-year $S_a(5\text{ s})$ when calculated by the Somerville–Abrahamson model. The proposed model shows different spatial patterns of amplification than the Somerville–Abrahamson model; it is believed that these differences are in large part due to refinements to the relationship between source-to-site geometry and directivity effects resulting from the increased observational data obtained since publication of the Somerville *et al.* (1997) model. Results such as these provide useful information regarding the range of distances over which one might expect directivity effects to play an important role in seismic hazard.

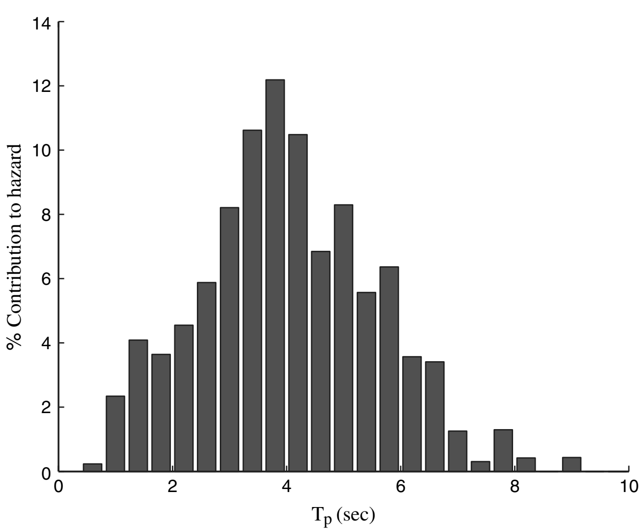

Figure 16. Deaggregation results showing the percent of contribution to hazard by T_p given $S_a(5\text{ s}) > 0.3$ g.

Deaggregation to Aid in Ground-Motion Selection

Ground motion selection for near-fault sites is a topic that is currently under investigation, and the output from the proposed procedure may be useful to studies of such selection. Ground motion selection for a site typically involves selecting and scaling a set of ground motions to represent the hazard conditions at the site. The ground motions selected for analysis of near-fault structures should include an appropriate number of pulselike ground motions to correctly represent the hazard conditions at site, and the framework presented here can aid in identifying appropriate ground motions for near-fault sites.

The number of pulselike ground motions in the set of selected ground motions should reflect the probability of observing a pulse at the site. The probability of observing a pulse, given that S_a exceeds a particular value, can be obtained from equation (27). Figure 15 shows the result of such hazard deaggregation for the site shown in Figure 5.

Deaggregation can also be used to find out the percentage contribution to hazard as a function of pulse period. Figure 16 shows the percentage contribution to 2% in 50-year $S_a(5\text{ s})$ hazard by different pulse periods. Figure 16 shows that there are a wide range of contributing pulse periods, which was expected because the presence of a pulse amplifies S_a over a range of periods. While selecting ground motions one should select pulselike motions with pulse periods that closely represent the distribution computed by deaggregation.

Conclusion

A framework to include the effects of pulselike ground motions in PSHA has been proposed. A standard ground-motion model was modified to account for the amplification in spectral acceleration due to the presence of pulselike ground motion and the overprediction of near-fault non-pulselike ground motions. To calibrate the modification, a dataset was built by first classifying each ground motion in the NGA database as pulselike or non-pulselike, and then studying their spectra separately.

The PSHA calculation was broken down into smaller problems of finding the probability of pulse occurrence at a site given the source-to-site geometry, the probability of occurrence of a pulse in a particular orientation at the site given pulselike ground motion is observed, the period of pulse expected at the site given the magnitude of earthquake, and the amplification of spectral acceleration given the period of an observed pulse at the site. These models were fitted using appropriate statistical techniques. All models and an algorithm to use these models to perform full PSHA computation were described. The framework is modular, which is desired because all the models will surely need to be updated in the future as more data and knowledge become available.

Example hazard computations were performed and the results from the approach proposed here were compared to predictions from the Somerville *et al.* (1997) model modified by Abrahamson (2000). The results from the two methods differ and will continue to be studied to verify that the model proposed here produces predictions more consistent with reality.

The proposed framework allows deaggregation of hazard to find the probability of observing a pulselike ground motion given a particular level of S_a is exceeded and the distribution of associated pulse periods. These deaggregation results are not available when using the Somerville–Abrahamson approach. These results lead to a deeper understanding of near-fault hazard and may aid in selecting appropriate ground motions for near-fault sites.

Data and Resources

The earthquake ground-motion recordings used in this study came from the Next Generation Attenuation (NGA) database (Chiou *et al.*, 2008). The database is accessible online at http://peer.berkeley.edu/nga/ (last accessed January 2011).

Acknowledgments

Thanks to Iunio Iervolinio for helpful explanation of the Iervolino and Cornell (2008) model and his detailed review of the paper. This material is based upon work supported by the National Science Foundation under NSF grant number CMMI 0726684. Any opinions, findings, and conclusions or recommendations expressed in this material are those of the authors and do not necessarily reflect the views of the National Science Foundation.

References

Abrahamson, N. A. (2000). Effects of rupture directivity on probabilistic seismic hazard analysis, In *Sixth International Conf. Seismic Zonation*, Oakland, California. Earthquake Engineering Research Inst.

Akkar, S., U. Yazgan, and P. Gulkan (2005). Drift estimates in frame buildings subjected to near-fault ground motions, *J. Struct. Eng.* **131,** no. 7, 1014–1024.

Alavi, B., and H. Krawinkler (2001). Effects of near-fault ground motions on frame structures, Technical Report Blume Center Report 138, Stanford, California.

Anderson, J. C., and V. Bertero (1987). Uncertainties in establishing design earthquakes, *J. Struct. Eng.* **113,** no. 8, 1709–1724.

Baker, J. W. (2007). Quantitative classification of near-fault ground motions using wavelet analysis, *Bull. Seismol. Soc. Am.* **97,** no. 5, 1486–1501.

Benjamin, J. R., and C. A. Cornell (1970). *Probability, Statistics, and Decision for Civil Engineers*, McGraw-Hill, New York.

Bertero, V., S. Mahin, and R. Herrera (1978). Aseismic design implications of near-fault San Fernando earthquake records, *Earthquake Eng. Struct. Dynam.* **6,** no. 1, 31–42.

Boore, D. M., and G. M. Atkinson (2007). Boore–Atkinson NGA ground motion relations for the geometric mean horizontal component of peak and spectral ground motion parameters, Technical report, Pacific Earthquake Engineering Research Center, Berkeley, California.

Boore, D. M., and G. M. Atkinson (2008). Ground-motion prediction equations for the average horizontal component of PGA, PGV, and 5%-damped PSA at spectral periods between 0.01 s and 10.0 s, *Earthquake Spectra* **24,** no. 1, 99–138.

Bray, J. D., and A. Rodriguez-Marek (2004). Characterization of forward-directivity ground motions in the near-fault region, *Soil Dynam. Earthquake Eng.* **24,** no. 11, 815–828.

Chioccarelli, E., and I. Iervolino (2010). Near-source seismic demand and pulse-like records: A discussion for L'Aquila earthquake, *Earthquake Eng. Struct. Dynam.* **39,** no. 9, 1039–1062.

Chiou, B., R. Darragh, N. Gregor, and W. Silva (2008). NGA project strong-motion database, *Earthquake Spectra* **24,** no. 1, 23–44.

Fu, Q., and C. Menun (2004). Seismic-environment-based simulation of near-fault ground motions, In *Proc. 13th World Conference on Earthquake Engineering*, Vancouver, Canada, 15 pp.

Hall, J. F., T. H. Heaton, M. W. Halling, and D. J. Wald (1995). Near-source ground motion and its effects on flexible buildings, *Earthquake Spectra* **11,** no. 4, 569–605.

Howard, J. K., C. A. Tracy, and R. G. Burns (2005). Comparing observed and predicted directivity in Near-Source ground motion, *Earthquake Spectra* **21,** no. 4, 1063–1092.

Iervolino, I., and C. A. Cornell (2008). Probability of occurrence of velocity pulses in near-source ground motions, *Bull. Seismol. Soc. Am.* **98,** no. 5, 2262–2277.

Iwan, W. (1997). Drift spectrum: Measure of demand for earthquake ground motions, *J. Struct. Eng.* **123,** no. 4, 397–404.

Kramer, S. L. (1996). *Geotechnical Earthquake Engineering*, Prentice Hall, Upper Saddle River, New Jersey.

Kutner, M. H., C. Nachtsheim, and J. Neter (2004). *Applied Linear Regression Models*, McGraw-Hill/Irwin, Boston; New York.

Luco, N., and C. A. Cornell (2007). Structure-specific scalar intensity measures for near-source and ordinary earthquake ground motions, *Earthquake Spectra* **23,** no. 2, 357–392.

Makris, N., and C. J. Black (2004). Dimensional analysis of bilinear oscillators under pulse-type excitations, *J. Eng. Mech.* **130,** no. 9, 1019–1031.

Mavroeidis, G. P., G. Dong, and A. S. Papageorgiou (2004). Near-fault ground motions, and the response of elastic and inelastic single-degree-of-freedom (SDOF) systems, *Earthquake Eng. Struct. Dynam.* **33,** no. 9, 1023–1049.

Mavroeidis, G. P., and A. S. Papageorgiou (2003). A mathematical representation of near-fault ground motions, *Bull. Seismol. Soc. Am.* **93,** no. 3, 1099–1131.

McGuire, R. K. (2004). *Seismic Hazard and Risk Analysis*, Earthquake Engineering Research Institute, Berkeley, California.

Menun, C., and Q. Fu (2002). An analytical model for near-fault ground motions and the response of SDOF systems, in *Proc. 7th U.S. National Conf. Earthquake Engineering*, Boston, Massachusetts, 10 pp.

Somerville, P. G. (2003). Magnitude scaling of the near fault rupture directivity pulse. *Phys. Earth Planet. In.* **137,** no. 1, 201–212.

Somerville, P. G. (2005). Engineering characterization of near fault ground motion. *2005 New Zealand Society for Earthquake Engineering Conference*, *Taupo, New Zealand*, 8 pp.

Somerville, P. G., N. F. Smith, R. W. Graves, and N. A. Abrahamson (1997). Modification of empirical strong ground motion attenuation relations to include the amplitude and duration effects of rupture directivity, *Seismol. Res. Lett.* **68,** no. 1, 199–222.

Spudich, P., and B. S. J. Chiou (2008). Directivity in NGA earthquake ground motions: Analysis using isochrone theory, *Earthquake Spectra* **24,** no. 1, 279–298.

Tothong, P., C. A. Cornell, and J. W. Baker (2007). Explicit-directivity-pulse inclusion in probabilistic seismic hazard analysis, *Earthquake Spectra* **23,** no. 4, 867–891.

Wells, D. L., and K. J. Coppersmith (1994). New empirical relationships among magnitude, rupture length, rupture width, rupture area, and surface displacement. *Bull. Seismol. Soc. Am.* **84,** no. 4, 974–1002.

Youngs, R. R., and K. Coppersmith (1985). Implications of fault slip rates and earthquake recurrence models to probabilistic seismic hazard analysis, *Bull. Seismol. Soc. Am.* **75,** no. 4, 939–964.

Department of Civil and Environmental Engineering
John A. Blume Earthquake Engineering Center
Stanford University
Building 540, Room 206
Stanford, California 94305
shrey@stanford.edu
(S.K.S.)

Department of Civil and Environmental Engineering
Stanford University
Stanford, California 94305
bakerjw@stanford.edu
(J.W.B.)

Manuscript received 8 April 2010